Chinese Chemical Letters 37 (2026) 112788

Contents lists available at ScienceDirect

Chinese Chemical Letters

journal homepage: www.elsevier.com/locate/cclet

Highly matched NbN-TiN nano-heterocrystals immobilized in hollow porous N-doped carbon framework to achieve high-performance lithium–sulfur batteries

Xiaoran Li[a], Wenqian Liu[b], Liwei Zhu[a], Yichun Gu[a], Changhui Sun[a], Peng Wang[c], Baojuan Xi[c], Shenglin Xiong[c], Nianxiang Shi[a,*]

[a] School of Chemistry and Chemistry Engineering, Qilu Normal University, Ji'nan 250200, China
[b] College of Preschool Education, Qilu Normal University, Ji'nan 250200, China
[c] School of Chemistry and Chemical Engineering, Shandong University, Ji'nan 250100, China

ARTICLE INFO

Article history:
Received 23 January 2026
Revised 15 April 2026
Accepted 16 April 2026
Available online 16 April 2026

Keywords:
NbN/TiN heteroccrystal
Shuttling effect
High lattice matching
Built–in electric field
Lithium–sulfur batteries

ABSTRACT

Commercialization of rechargeable lithium–sulfur batteries (LSBs) is severely hindered by the "shuttle effect" and their sluggish electrochemical kinetics. Herein, highly matched NbN/TiN heterocrystals with nanosize (<5 nm) uniformly dispersed within in hollow porous N–doped carbon microspheres (NbN/TiN@N–C) was designed. DFT calculations and electrochemical tests demonstrate the remarkable improvement in anchoring lithium polysulfides (LiPSs) and sulfur redox kinetics. Specifically, the hollow porous frameworks can physically confine LiPSs and effectively alleviate volume changes, and simultaneously the immobilized NbN/TiN nanocrystals can strongly interact with LiPSs by the dual–chemical adsorption that the formation of Nb–S and Ti–S bonds. The nanosized NbN/TiN heterocrystals and their clusters induce maximum reaction surface and numerous activity sites. Significantly, the heterocrystals, based on high lattice matching and stable built–in electric field, endows smooth channels for Li^+ diffusion and maximum electron transfer ability to catalysts. The LSBs with NbN/TiN@N–C separator delivers ultralong cycling stability that sustained 545.5 mAh/g with only 0.056 % capacity decay per cycle over 1000 cycles at 2 C and high rate performance with 663.7 mAh/g at 10 C. This work provides a novel insight for regulating LiPSs through highly matched binary heterogeneous catalyst to advance the industrial application of LSBs.

© 2026 Published by Elsevier B.V. on behalf of Chinese Chemical Society and Institute of Materia Medica, Chinese Academy of Medical Sciences.

Lithium–sulfur batteries (LSBs), as a promising next–generation clean energy system, have attracted tremendous research interest due to their ultrahigh energy density (≈2600 Wh/kg) and theoretical specific capacity (1675 mAh/g) [1–3]. Moreover, sulfur is an abundant, low–cost, and environmentally benign cathode material [4,5]. Despite these intrinsic merits, the practical application of LSBs is impeded by several critical challenges, including sluggish reaction kinetics caused by the insulating nature of Li_2S and sulfur, the notorious shuttle effect originating from soluble lithium polysulfides (LiPSs) in organic electrolytes, and poor cycling stability resulting from severe volume fluctuations and uneven Li_2S deposition [6–8]. Tremendous efforts including electrolyte optimization, nanostructure design, and separator modification have been devoted to address these limitations, particularly through the incorporation of functional solid additives on the cathode or separator [9–12]. These additives based on their functions can be broadly classified into adsorbents, mediators, and catalysts. Nevertheless, the adsorbents have strong adsorption function without catalytic activity, which struggles to solve the kinetic problems of polysulfide conversion [9,10]. In addition, soluble mediators facilitate homogeneous LiPSs conversion in the electrolyte but suffer from uncontrolled dissolution and potential contamination of the lithium anode [11,12]. Comparatively, heterogeneous catalysts integrate strong LiPSs anchoring and the catalytic capability to reduce energy barrier of the conversion proceed from LiPSs to Li_2S, which has been confirmed as a promising strategy to realize high performance LSBs.

Nanostructure engineering and heteroatom doping have been widely employed to enhance the overall electrochemical performance of LSBs. The strategy combining morphology regulation (*e.g.*, construction of hollow porous structures) with nitrogen doping can significantly buffer volume change and promote electrolyte penetration through the cavity framework [13,14]. Besides, the

* Corresponding author.
E-mail address: chesnx@qlnu.edu.cn (N. Shi).

https://doi.org/10.1016/j.cclet.2026.112788
1001-8417/© 2026 Published by Elsevier B.V. on behalf of Chinese Chemical Society and Institute of Materia Medica, Chinese Academy of Medical Sciences.

porous architecture provides rapid diffusion "highway" for ions, effectively shortening ions diffusion pathways and reducing diffusion impedance. Meanwhile, the incorporation of nitrogen atoms improves electrical conductivity and polysulfide affinity of carbon-based sulfur host materials, which reduces interfacial transport resistance and boosts charge transfer. However, the chemical adsorption capability solely relying on the polar sites generated by nitrogen doping struggles to completely suppress the shuttle effect because of the limited anchoring effect on polysulfides. Thus, many researchers have focused to introducing polar materials (*i.e.*, TiC, VN, MoS_2, CoP), which possess stronger chemisorption for LiPSs and simultaneously exert rapid trapping–conversion effects [15–18]. Tiranium nitride, featuring superior conductivity, moderate density, and robust mechanical stength, is widely studied for its strong polysulfide adsorption capability derived from polar N–Ti bonds [19,20]. Meanwhile, niobium nitride, characterized by excellent electronic conductivity and chemical stability, can strongly anchor LiPSs through Nb–S bond formation and catalyze their reduction to Li_2S [21]. Nevertheless, they all fall short of ideal performance in LSBs due to insufficient active sites of limited surface area. Besides, single-component catalysts exhibit inherent limitations in anchoring LiPSs and accelerating their redox reactions. Encouragingly, the heterostructure can construct robust interfacial interactions and intrinsic built–in electric fields, generate abundant active sites, significantly enhance the capability to immobilize LiPSs, and synergistically promote their rapid conversion [22,23].

The constructed heterointerfaces typically exhibit enhanced catalytic activity owing to electronic redistribution and interaction between components with different Fermi levels upon contact [24,25]. Moreover, the interfacial coupling within binary heterostructures generates an internal electric field that promotes charge transfer between the catalyst and LiPSs, thereby optimizing adsorption energies and accelerating multistep LiPSs conversion kinetics [26,27]. For instance, Song *et al.* developed a RuP_2–RuP heterostructure that provided abundant active sites and modulated electron transport across the interface, exhibiting excellent electrocatalytic performance toward LiPSs conversion [28]. However, current research predominantly prefers to choose heterojunctions with low lattice compatibility. Although this can introduce strain or vacancy defects to increase active sites, it may also trigger issues like interfacial instability and increased internal resistance. Moreover, the catalytic performance of materials generally undergoes a remarkable enhancement when their particle sizes are reduced down to the nanoscale [29]. Therefore, developing a tailored strategy to fabricate a nano heterostructure material with high binary lattice compatibility to form coherent crystal planes is meaningful. This can effectively reduce interface defects, provide a "highway" for rapid charge transfer, and is the key to reducing battery internal resistance and improving rate performance [30]. Besides, excellent lattice matching can maintain the structural integrity of heterojunctions during long–term cycles, preventing nanoparticle aggregation and deactivation. At present, there are rarely few investigations to exploring the application of high lattice matching heterojunctions in LSBs, and controlling the stable surface of heterostructure catalyst to optimize long–life cycle remains significant obstacles.

Based on the above considerations, we proposed N–doped hollow porous carbon microspheres embedded by uniformly NbN–TiN nano–heterocrystals (NbN/TiN@N–C), which enables high stability catalyst surface for strong immobilization and conversion of LiPSs. The robust architectures and evenly encapsulated heterocrystals hold synergistic effects of physical confinement, physisorption and dual chemisorption of Nb–S/Ti–S bonds on LiPSs, effectively suppressing volume expansion and shuttle effect. Besides, TiN acts as a rigid support, forming a binary nano–heterocrystals that features high lattice matching to stable built–in electric field and

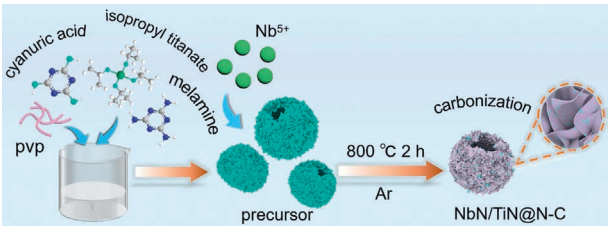


Fig. 1. Schematic illustration of the preparation procedure of the hollow–porous–flower–like NbN/TiN@N–C heterostructure.

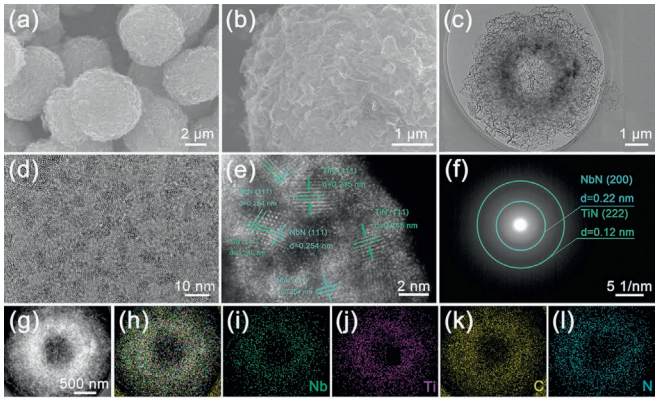


Fig. 2. Morphology and structure of the hollow–porous–flower–like NbN/TiN@N–C heterostructure. (a, b) SEM and (c) TEM images. (d) HRTEM images. (e) HAADF–STEM images. (f) The selected area electron diffraction (SAED) pattern. (g–l) FESEM image and the corresponding EDS maps of Nb, Ti, C, and N.

smooth ion diffusion pathways. The heterocrystals and their clusters permeate the matrix, maximizing the exposure of reactivity sites and improving internal ion/electron migration. Consequently, LSBs employing the NbN/TiN@N–C separator delivers long–term cycling stability (827.6 mAh/g at 1 C after 500 cycles and 545.5 mAh/g at 2 C after 1000 cycles) and outstanding rate capability (663.7 mAh/g at 10 C). This comprehensive study provides a rational design approach for constructing binary heterogeneous catalysts to address the challenges in commercialization of LSBs.

Fig. 1 illustrated the synthesis process of NbN/TiN@N–C through facile template and annealing methods, and the detailed fabrication process is shown in Experimental Section in Supporting information. The morphology and microstructure of the obtained samples were characterized by FESEM and TEM. As shown in Figs. S1 and S2 (Supporting information), the precursors of NbN/TiN@N–C, NbN@N–C, and TiN@N–C all exhibit hierarchical flower–like microspherical architectures, confirming the successful templating effect derived from the polymerization of melamine and cyanuric acid. Figs. 2a–c reveal that NbN/TiN@N–C retains the morphology of its precursor while presenting thinner nanosheets and a highly open porous structure, which facilitates electrolyte infiltration and provides abundant active sites for electrochemical reactions. Similar morphology retention after annealing is observed for NbN@N–C and TiN@N–C (Fig. S3 in Supporting information). HRTEM (Fig. 2d) further demonstrates that nanosized NbN and TiN particles (<5 nm) are uniformly distributed on the nitrogen–doped carbon framework. The high–angle annular dark–field scanning TEM (HAADF–STEM) image (Fig. 2e) reveals lattice spacings of 0.245 nm and 0.254 nm, corresponding to the (111) planes of TiN and NbN, respectively. Notably, the lattice stripes at the interface of heterogeneous are continuous and dislocation free enabled by high lattice matching of TiN and NbN, indicating the formation of coherent crystal planes [30]. The presence of coherent crystal plane confirms the successful formation of tightly coupled NbN/TiN het-

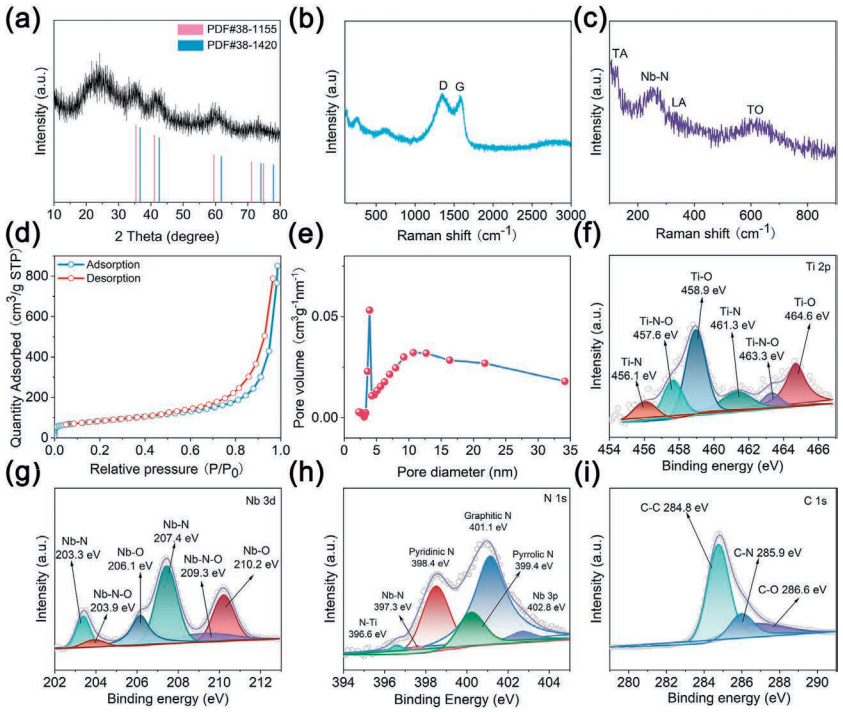


Fig. 3. The phase and compositions of the hollow–porous–flower–like NbN/TiN@N–C heterostructure. (a) XRD pattern. (b, c) Raman spectrum. (d) N_2–adsorption–disorption profile. (e) The pore distribution. (f–i) XPS spectra of Ti 2p, Nb 3d, N 1s, and C 1s.

erocrystal. Additionally, numerous bright spots appearing beyond the lattice fringes indicate the generation of ample NbN and TiN nanoclusters during annealing. The selected–area electron diffraction (SAED) pattern (Fig. 2f) displays two diffraction rings corresponding to the (222) plane of TiN and the (200) plane of NbN, providing further evidence for heterocrystal formation. The corresponding EDS elemental mappings (Figs. 2g–l) confirm the homogeneous distribution of C, N, Nb, and Ti elements throughout the NbN/TiN@N–C framework.

Power X–ray diffraction (XRD) analysis was first performed to identify the TiN and NbN phases in the NbN/TiN@N–C heterostructure. As shown in Fig. 3a, the principal diffraction peaks located at 35.4°, 41.1°, and 59.5° correspond to the (111), (200), and (220) planes of the NbN phase (JCPDS No. 38–1155), respectively. Meanwhile, the peaks observed at 36.7°, 42.6°, 61.8°, and 78.0° are indexed to the (111), (200), (220), and (222) planes of the TiN phase (JCPDS No. 38–1420). The relatively broad diffraction peaks can be ascribed to the small crystallite size of the obtained nanoparticles [21]. In addition, the broad feature at approximately 26° is assigned to the (002) diffraction of amorphous carbon. The XRD patterns of NbN@N–C and TiN@N–C (Fig. S4 in Supporting information) display well–defined peaks that match well with their respective standard reference cards. The coexistence of well–resolved and diffraction peaks corresponding to both TiN and NbN phases in NbN/TiN@N–C confirms the successful formation of a high–purity NbN/TiN heteroccrystal, which aligns with STEM and SAED results. Raman spectroscopy was further employed to investigate the carbonaceous framework of the composites (Figs. 3b and c). Two prominent bands centered at 1349 and 1588 cm^{-1} are attributed to the disorder (D) band and graphitic (G) band, respectively. The intensity ratio of them indicates the presence of substantial structural defects, which can be attributed to heterojunction formation and N–doping within the carbon matrix [31]. Additionally, a broad band near 228 cm^{-1} is assigned to the Nb–N stretching vibration, while other peaks located within the ranges of 400–700, 280–360, and 130–240 cm^{-1} correspond to the transverse optical, longitudinal acoustic, and transverse acoustic vibration modes of TiN, respectively [19,32,33]. The porous structural characteristics of NbN/TiN@N–C were analyzed using N_2 adsorption–desorption isotherms and Barret–Joyner–Halenda (BJH) pore–size distribution curves. As shown in Fig. 3d, the isotherm exhibits a typical type–IV hysteresis loop in the relative pressure range of 0.4–1.0 P/P_0, indicative of a mesoporous structure. The Brunauer–Emmett–Teller (BET) specific surface area of NbN/TiN@N–C is calculated to be 293.9 m^2/g. Notably, the distinct adsorption at low relative pressure suggests the presence of abundant micropores, while the pore–size distribution (Fig. 3e) indicates that the majority of pores fall within the 3–12 nm range, with an average diameter of approximately 4 nm. Such a hierarchically porous architecture, coupled with a high surface area, can facilitate electrolyte infiltration, provide sufficient active sites for full redox reactions, effectively confine soluble LiPSs, and accelerate their conversion kinetics by enhancing ion diffusion and electron transport.

The surface element composition and valence states of Nb, Ti, N, and C in NbN/TiN@N–C were investigated by X–ray photoelectron spectroscopy (XPS), as shown in Figs. 3f–i. The high–resolution Ti 2p spectrum exhibits six characteristic peaks located at 456.1 (461.3), 457.6 (463.3), and 458.9 (464.6) eV, corresponding to Ti–N, Ti–N–O, and Ti–O bonds, respectively [34,35]. The presence of Ti–O species indicates partial surface oxidation of TiN upon air exposure [34]. In the Nb 3d spectrum, three spin–orbit doublets are observed, corresponding to Nb^{3+} and Nb^{5+}oxidation states. The peaks at 203.3, 203.9, and 206.1 eV are assigned to Nb^{3+}–N, Nb–N–O, and Nb^{5+}–O components for Nb $3d_{5/2}$, while the accompanying peaks at 207.4, 209.3, and 210.2 eV correspond to Nb $3d_{3/2}$ binding energies [36,37]. These results indicate that partial oxidation of NbN also occurred on the surface, similar to TiN [21]. The N 1s spectrum displays three peaks at 396.6, 397.3, and 402.8 eV, which can be attributed to N–Ti, Nb–N, and Nb 3p signals, confirming the coexistence of NbN and TiN phases. Additional peaks at 398.4, 399.4, and 401.1 eV correspond to pyridinic–N, pyrrolic–N, and graphitic–N species, respectively, indicating successful N–doping within the

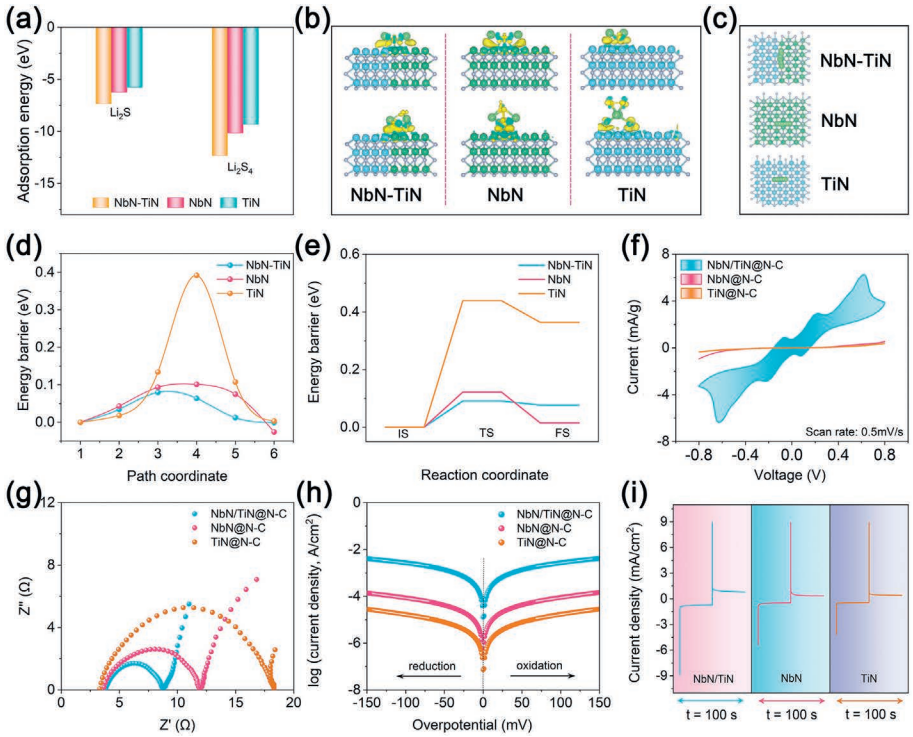


Fig. 4. (a) Calculated adsorption energies of Li_2S/Li_2S_4 on NbN–TiN, NbN and TiN. (b) Difference in charge density of Li_2S/Li_2S_4 adsorption using various catalysts. (c) The ionic migration pathways of various catalysts. (d) The Li^+ migration energy barrier for three kinds of pathways. (e) Li_2S decomposition energy barrier on various catalyst surfaces. (f) CV curves of different symmetric cells at a scan rate of 0.5 mV/s. (g) EIS spectra of different symmetric cells. (h) The Tafel plots of various catalysts. (i) Chronoamperometric curves for various catalysts.

carbon matrix [19,21]. The C 1s spectrum shows a dominant peak at 284.4 eV corresponding to C–C bonding, accompanied by weaker peaks at 285.9 and 286.6 eV, which are assigned to C–N and C–O bonds, respectively [19]. Quantitative elemental analysis by ICP–AES indicates reveals that the Nb and Ti contents in NbN/TiN@N–C are approximately 18.5 wt% and 10.2 wt%, respectively. Complementary thermogravimetric analysis (TGA) results (Fig. S5 in Supporting information) indicate a carbon content of 65.5 wt%. Furthermore, the sulfur content of the cathode material is estimated to be 72.1 wt%.

The functionalized interlayer must maintain robust mechanical integrity with the separator substrate to dynamically accommodate the strain effects arising from cathode volume expansion during cycling. Fig. S6 (Supporting information) demonstrates that the NbN/TiN@N–C layer exhibits excellent adhesion to the PP membrane during folding/recovery tests. Furthermore, Fig. S7 (Supporting information) presents top and cross–sectional SEM images of NbN/TiN@N–C, NbN@N–C, and TiN@N–C–coated PP separators, revealing that the coatings are uniformly distribute on the PP separator surface without delamination, with thicknesses of 10, 12, and 11 μm, respectively. The interfacial wetting behavior, as evaluated by contact–angle measurements (Fig. S8 in Supporting information), indicates the electrolyte infiltration capacity: NbN/TiN@N–C–coated PP > NbN@N–C–coated PP > TiN@N–C–coated PP. The NbN/TiN@N–C modified interlayer displays a superwetting surface ($\theta \approx 0°$), indicating that the electrolyte has a high permeation, which is conducive to the superior charge transport over the catalyst surface.

The LiPS adsorption capabilities of NbN/TiN@N–C, NbN@N–C, and TiN@N–C were evaluated through visual assays using a Li_2S_6 electrolyte as a representative substance. As shown in Fig. S9 (Supporting information), the solution containing NbN/TiN@N–C almost completely loses its brown color, while the solutions containing NbN@N–C and TiN@N–C retain varying degrees of yellow coloration after 12 h, with NbN@N–C exhibiting a stronger adsorption effect than TiN@N–C. This result confirms that NbN/TiN@N–C can effectively absorb LiPSs, mitigating the shuttle effect to a greater extent. The anchoring function of the different sulfur host materials, including NbN/TiN, NbN, and TiN, toward Li_2S and Li_2S_4 was further investigated through DFT calculations. Fig. S10 (Supporting information) shows the optimized configurations of Li_2S and Li_2S_4 adsorbed on NbN–TiN, NbN, and TiN, indicating that sulfur species are well–anchored on these substrates, supporting the rational design of the NbN–TiN heterostructure. In these configurations, Nb and Ti sites interact with sulfur atoms to form Nb–S and Ti–S bonds, respectively, ensuring stable adsorption. The calculation results demonstrates that NbN–TiN (–7.37 and –12.35 eV) exhibits superior binding energy toward Li_2S and Li_2S_4 compared to NbN (–6.25 and –10.16 eV) and TiN (–5.77 and –9.32 eV) (Fig. 4a). Additionally, NbN shows stronger adsorption than TiN. The binding interactions of these catalysts with Li_2S and Li_2S_4 were further explored through differential charge density analysis (Fig. 4b). The results reveal that NbN–TiN exhibits substantial charge accumulation at the binding sites, leading to stronger interactions with Li_2S/Li_2S_4. This enhanced adsorption facilitates rapid electron transfer, thereby improving electrocatalytic activity for polysulfide conversion. Crucially, NbN–TiN promotes charge transfer at the terminal S atoms by forming Nb–S and Ti–S bonds, which synergistically strengthens the adsorption of polysulfide anions through interfacial coupling. This dual–anchoring mechanism enriches both the chemical anchoring sites and catalytic active centers, enhancing the overall performance of the composite.

The rapid diffusion of lithium ions is crucial for mitigating critical issues such as polysulfide shuttling and lithium dendrite growth, as well as optimizing reaction kinetics. Fig. 4c simulates the migration paths of Li^+ in NbN–TiN, NbN, and TiN. The calculations reveal that NbN–TiN exhibits the lowest Li^+ migration energy barrier, thereby most effectively promoting sulfur lithia-

tion/delithiation kinetics and suppressing shuttle effects (Fig. 4d). Additionally, Fig. S11 (Supporting information) shows the diffusion paths of Li_2S on NbN–TiN, NbN, and TiN, as simulated by DFT calculations. The decomposition energy barrier for Li_2S on NbN–TiN (0.09 eV) is significantly lower than that on NbN (0.12 eV) and TiN (0.44 eV), suggesting that interfacial electronic coupling at the NbN–TiN heterojunction accelerates sulfur redox kinetics and reduces the accumulation of sulfur species (Fig. 4e).

To evaluate the efficiency of different catalysts in facilitating LiPS conversion, various kinetic tests were performed using symmetric cells. As shown in Fig. 4f, the current density of the NbN/TiN@N–C symmetric cell is significantly higher than that of NbN@N–C and TiN@N–C, indicating superior catalytic performance in promoting the rapid conversion of LiPSs. Furthermore, three distinct reduction peaks at 0.07, –0.23, and –0.62 V correspond to the stepwise conversion process ($S_8 \rightarrow S_6^{2-}$; $S_6^{2-} \rightarrow S_4^{2-}$; $S_4^{2-} \rightarrow S^{2-}$), with oxidation peaks observed at –0.07, 0.23, and 0.62 V, representing the reverse reactions [26]. These peaks are clearly visible for NbN/TiN@N–C but are less pronounced for NbN@N–C and TiN@N–C. The charge transport within the electrode material is closely related to its intrinsic electrical conductivity. To assess this, Fig. 4*g* presents the EIS results of symmetric cells with the three catalysts. NbN/TiN@N–C demonstrates a smaller charge transfer resistance, facilitating faster redox conversion. The charge transfer resistence of NbN/TiN@N–C (4.76 Ω) is lower than that of NbN@N–C (8.33 Ω) and TiN@N–C (14.84 Ω), confirming its superior electrical conductivity. Further insights into the LiPSs conversion kinetics were obtained through Tafel analysis (Fig. 4h). The exchange current densities (i_0) calculated from the linear fitting of the partial Tafel region indicate that the NbN/TiN@N–C electrode has an outstanding i_0 of 1.05 mA/cm^2 for reduction and 1 mA/cm^2 for oxidation, significantly higher than the values for NbN@N–C (0.003 mA/cm^2 for reduction and 0.0029 mA/cm^2 for oxidation) and TiN@N–C (5.13×10^{-3} mA/cm^2 for both reduction and oxidation). Finally, chronoamperometry curves (Fig. 4i) from Li_2S_6 symmetric batteries with the three catalysts demonstrate that the current response is notable, indicating the detected current mainly arises from lithiation/delithiation reaction rather than double-layer capacitance [38]. Meanwhile, the current response for NbN/TiN@N–C electrode is the highest and further confirms its superior LiPSs conversion capability. The enhanced catalytic activity can be attributed to interfacial electron redistribution and synergistic catalytic effect induced by the NbN/TiN heterostructure, effectively lowering the energy barrier for LiPSs conversion and accelerating their redox reaction kinetics.

The deposition and dessolution behaviors of Li_2S were investigated through potentiostatic discharge and charge tests to evaluate the catalytic activity of materials for rapid bidirectional liquid–solid conversion of LiPSs. As shown in Fig. S12 (Supporting information), the Li_2S deposition capacity for NbN/TiN@N–C is 304 mAh/g, which is higher than that of NbN@N–C (268 mAh/g) and TiN@N–C (242 mAh/g). This enhanced capacity is attributed to the superior adsorption ability and catalytic activity of the NbN/TiN@N–C heterostructure. Additionally, the deposition peak for NbN/TiN@N–C is observed at 190 s, much earlier than the deposition peaks for NbN@N–C (228 s) and TiN@N–C (242 s), indicating faster nucleation of Li_2S (Fig. S12). Corresponding Li_2S dessolution measurements were performed to evaluate the catalytic performance, as shown in Fig. S13 (Supporting information). The Li_2S dissolution capacity for NbN/TiN@N–C is 591 mAh/g, which is significantly higher than the capacities for NbN@N–C (580 mAh/g) and TiN@N–C (537 mAh/g). Furthermore, the dissolution peak for NbN/TiN@N–C occurs the earliest at 221 s, while those for NbN@N–C and TiN@N–C appear later at 385 s and 351 s, respectively. These results demonstrate the superior Li_2S dessolution and catalytic activity of NbN/TiN@N–C. To further assess the deposition and dessolution kinetics of Li_2S, the are Ak^2 values were calculated using the equation $Ak^2 = 2/(\pi t_m^3)$, where higher Ak^2 values indicate faster deposition and dessolution rates [38,39]. As shown in Fig. S14 (Supporting information), the Ak^2 values for NbN/TiN@N–C are 9.3×10^{-8} S^{-3} (deposition) and 5.4×10^{-8} S^{-3} (dissolution), which are significantly higher than those for NbN@N–C (5.4×10^{-8} S^{-3} and 1.1×10^{-8} S^{-3}) and TiN@N–C (4.5×10^{-8} S^{-3} and 1.5×10^{-8} S^{-3}), indicating that the NbN/TiN heterostructure can greatly accelerate the Li_2S nucleation and precipitation kinetics.

The superior catalytic performance of NbN/TiN@N–C for LiPS conversion prompted the assembly of coin–type Li–S batteries using different materials as separators and S/C composites as cathodes to evaluate their electrochemical behavior. Fig. 5a presents the initial five cyclic voltammetry (CV) curves for NbN/TiN@N–C at a scan rate of 0.1 mV/s and a voltage range of 1.7–2.8 V. Two distinct reduction peaks are observed: One at 2.27 V (Peak 1), associated with the conversion of S_8 to soluble long–chain LiPSs (Li_2S_n,$4 \le n \le 8$), and another at 2.03 V (Peak 2), corresponding to the formation of insoluble Li_2S_2/Li_2S [2]. An anodic peak at 2.40 V (Peak 3) corresponds to the oxidation of Li_2S_2/Li_2S to soluble Li_2S_n and back to sulfur [40]. Upon subsequent cycles, the reduction peaks shift to higher potentials, while the oxidation peaks shift to lower potentials, likely due to electrochemical activation processes [21]. Notably, the CV curves overlap after the second cycle, demonstrating the exceptional reversibility and stability of NbN/TiN@N–C. To gain deeper insight into the catalytic behavior, *in situ* X–ray diffraction (XRD) tests were performed to monitor the evolution of sulfur species during the discharge/charge process. As shown in Fig. 5b, the initial peaks at 22.7°, 26.4°, 27.4°, and 28.3° correspond to α–S_8 (JCPDS No 77–0145). During lithiation, the α–S_8 peaks gradually disappear, indicating the rapid transformation of sulfur into LiPSs. A new peak at 26.8°, corresponding to Li_2S, grows in intensity and reaches its maximum at 1.7 V. During charging, the Li_2S peak gradually fades, and β–S_8 peaks reappear, with the most distinct peaks observed at 2.8 V [22,41,42]. These results confirm that sulfur species undergo a reversible conversion process. The evolution of the *in–situ* XRD patterns demonstrates that the NbN/TiN@N–C heterojuction, with its interfacial electron coupling, facilitates superior phase transformation of sulfur species, thereby inhibiting the shuttle effect of LiPSs and enhancing sulfur utilization.

To further evaluate the lithium–ion diffusion kinetics, the lithium–ion diffusion coefficient (D_{Li^+}) was calculated using the following Randles–Sevick equation [43,44]:

$$I_p = (2.69 \times 10^5) n^{1.5} A D_{Li^+}{}^{0.5} C v^{0.5} \quad (1)$$

where I_p represents the peak current, n is the number of electrons transferred during the redox reaction, A (cm^2) is the electrode area, D_{Li^+} (cm^2/s) is the Li^+ diffusion coefficient, C (mol/cm^3) is the concentration of Li^+ in the electrolyte, and v (V/s) is the scan rate. Among these parameters, n, A, and C are constants [45]. As shown in Fig. 5c, the calculated D_{Li^+} values for NbN/TiN@N–C are 1.66×10^{-8} cm^2/s (Peak 1) and 2.12×10^{-8} cm^2/s (Peak 3), which are significantly higher than those of NbN@N–C and TiN@N–C. This result clearly demonstrates that the NbN/TiN@N–C offers the most favorable Li^+ transport kinetics, attributed to the stable electric field effect between NbN and TiN that promotes efficient redox charge transfer. Additionally, the galvanostatic intermittent titration technique (GITT) was conducted to further quantify Li^+ diffusion and polysulfide conversion kinetics (Fig. 5d). Based on the correlation between overpotential and pulse current response, the internal reaction resistances of the three cells during the discharge–charge cycles were calculated. As shown in Figs. 5e and f, the NbN/TiN@N–C–based cell exhibits the lowest reaction resistance compared to NbN@N–C and TiN@N–C, confirming that

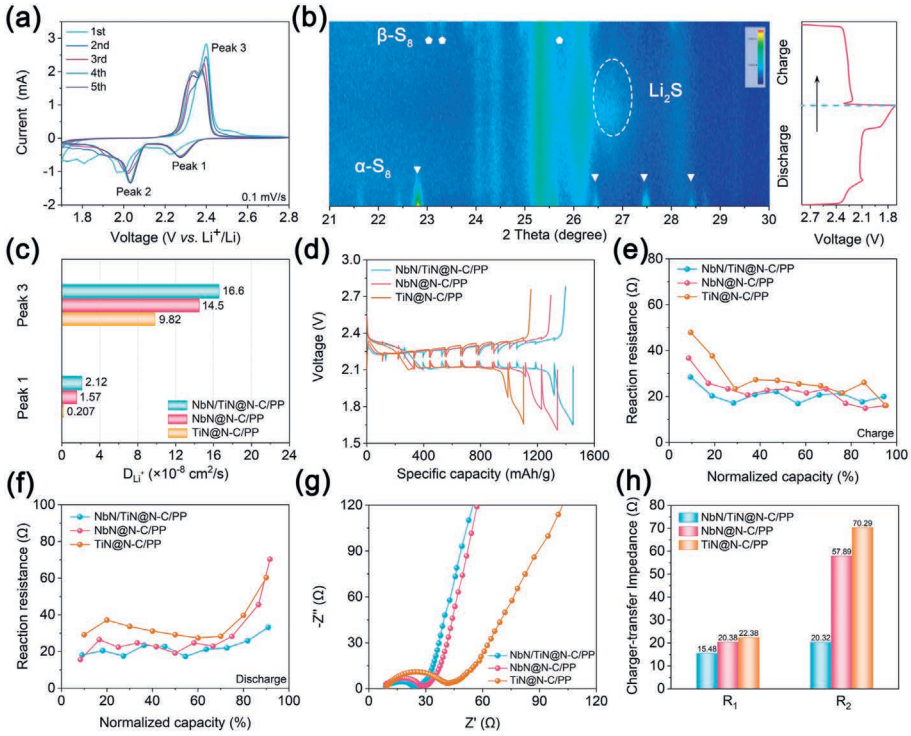


Fig. 5. (a) The CV curves of NbN/TiN@N–C based cell at 0.1 mV/s. (b) *In situ* XRD patterns of NbN/TiN@N–C and the corresponding charge/discharge curve. (c) The summary diagram of D_{Li^+} for various based LSBs. (d) GITT voltage profiles. (e) Discharge reaction resistance. (f) Charge reaction resistance. (g) EIS spectra of various based LSBs after cycling. (h) The summary diagram of charge–transfer impedance for various based LSBs.

the NbN/TiN@N–C facilitates faster Li_2S activation and nucleation. These results are consistent with the preceding electrochemical analyses and further validate the superior catalytic performance of NbN/TiN@N–C.

Electrochemical impedance spectra (EIS) was conducted to further investigate the enhanced redox kinetics of the cells with NbN/TiN@N–C, NbN@N–C, and TiN@N–C separators. As depicted in Fig. S15 (Supporting information), the NbN/TiN@N–C–based cell exhibits the lowest charger–transfer resistance (R_{ct}) in the high–frequency semicircle region before cycling, indicating superior interfacial charge–transfer ability and the corresponding equivalent circuit model is illustrated. Notably, after 10 cycles at 0.5 C, the impedance values of all cells decrease markedly, as shown in Fig. 5g, suggesting gradual electrode activation and improved electrolyte penetration. The detailed fitting results of charge–transfer kinetics for the different separators are summarized in Fig. 5h. Among them, the NbN/TiN@N–C–based cell presents the lowest R_1 and R_2 values, implying minimal resistance to ion and electron transport. Moreover, it also displays a smaller Warburg impedance coefficient, consistent with the higher Li^+ diffusion coefficient determined earlier (Fig. S16 in Supporting information) [46]. These results collectively confirm that the NbN/TiN heterostructure effectively accelerates electron transfer and enhances overall redox kinetics compared to the individual NbN and TiN counterparts. Furthermore, the ability of different separators to suppress the polysulfide shuttle effect was evaluated by self–discharge tests. As shown in Fig. S17 (Supporting information), all batteries were cycled at 0.5 C, followed by a resting period of 72 h at the 20th cycle, and then resumed cycling. The NbN/TiN@N–C–based cell maintained a capacity retention of 94.5 %, outperforming NbN@N–C (93.2 %) and TiN@N–C (92.3 %) under the same conditions. This superior capacity retention indicates that the NbN/TiN@N–C modified separator provides robust polysulfide anchoring and effectively restrains the shuttle effect, thereby ensuring stable cycling performance [47].

To fully explore the application potential of NbN/TiN@N–C, a series of tests were performed, leveraging its catalytic ability to accelerate sulfur conversion kinetics as demonstrated by both experimental and theoretical analyses. As shown in Fig. 6a, the long–time cycling performance of cells with different separators was evaluated at a current density of 0.5 C, with the first three cycles performed at 0.2 C for activation. The results reveal that the NbN/TiN@N–C–based cell achieves a higher initial discharge capacity of 1550.7 mAh/g at 0.2 C, outperforming the NbN@N–C (1459.6 mAh/g) and TiN@N–C (1377.3 mAh/g) cells. Notably, the NbN/TiN@N–C/PP cell maintains a reversible capacity of 667.7 mAh/g after 600 cycles, with a low capacity decay rate of 0.074 % per cycle, highlighting its excellent cycling stability. The high initial capacity and long–cycle stability are attributed to the stable adsorption and catalytic activity of the stable NbN/TiN heterocrystals. To further evaluate the cycling performance, the first charge–discharge curves at 0.5 C were analyzed after five pre–cycling cycles at 0.2 C for each separator. As shown in Fig. 6b, the discharge profile is characterized by two distinct phases: Q_H and Q_L. Q_H corresponds to the solid–liquid conversion of S_8 to soluble LiPSs, while Q_L is associated with the reduction of soluble LiPSs to the final product $Li_2S_{(2)}$ [48,49]. The discharge profile indicates that Q_L dominates the majority of the capacity contribution, identifying it as the rate–determination step. The Q_L/Q_H ratio is an important indicator for measuring the catalytic conversion speed of LiPSs. In this case, the NbN/TiN@N–C–based cell exhibits the highest Q_L/Q_H value of 2.33, outperforming NbN@N–C (2.14) and TiN@N–C (1.86), thus demonstrating superior performance in the liquid–solid conversion phase (Fig. 6c). Furthermore, the polarization potential (ΔE) of the NbN/TiN@N–C–based cell is 161 mV, which is significantly lower than that of NbN@N–C (176 mV) and TiN@N–C (188 mV), indicating better LiPSs redox reaction performance on the NbN/TiN heterostructure sites [50,51].

To further evaluate the performance of the different batteries, rate capability tests were conducted, as shown in Fig. 6d.

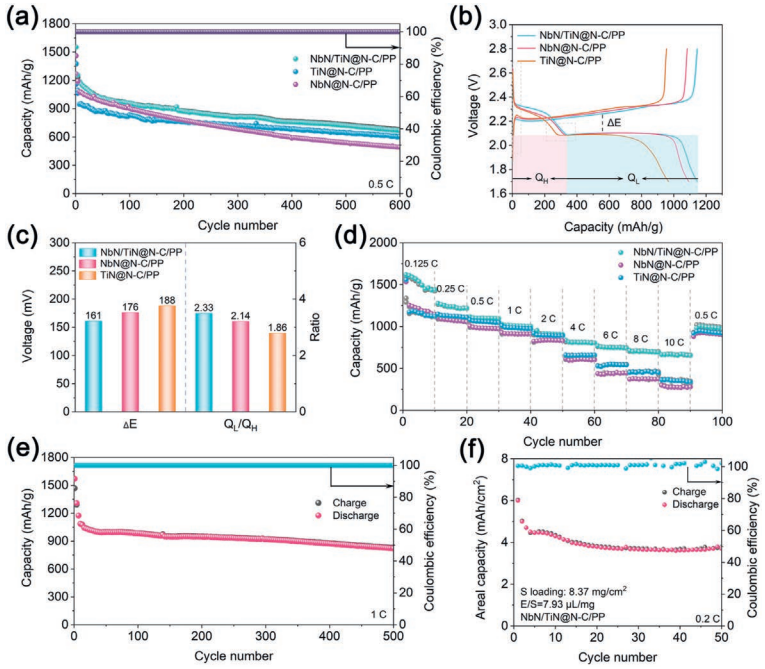


Fig. 6. (a) Cycling performance of different based LSBs at 0.5 C. (b) Charge/discharge curves at the current density of 0.2 C. (c) The ΔE and Q_L/Q_H values obtained from charge/discharge curves. (d) Rate performance for various based LSBs. (e) Cycling performance of NbN/TiN@N–C based LSBs at 1 C. (f) Cycling performance of NbN/TiN@N–C based LSBs with high sulfur loading at 0.2 C.

The NbN/TiN@N–C modified separator cell demonstrates excellent rate performance with reversible capacities of 1538.3, 1261.7, 1102.4, 1011.1, 911.7, 813, 753.5, 708.5, and 663.7 mAh/g at current densities of 0.125, 0.25, 0.5, 1, 2, 4, 6, 8, and 10 C, respectively. Notably, the cell recovers a substantial reversible capacity of 998.9 mAh/g when the current density is reduced back to 0.5 C, demonstrating its superior reversible performance. In contrast, the NbN@N–C and TiN@N–C–based cells show lower rate performance, underlining the enhanced catalytic and electronic properties of NbN/TiN@N–C. This outstanding rate capability is attributed to its moderate polysulfide adsorption and faster charge–transfer kinetics, facilitated by the interface electron coupling within the evenly distributed bimetallic heterojunction structure. The corresponding charge–discharge curves of the three cells at different rates, shown in Fig. S18 (Supporting information), further demonstrate that the NbN/TiN@N–C separator exhibits more stable charge/discharge plateaus, even at higher current densities. This stability is indicative of lower potential polarization, which enhances the cell's performance at high current densities. As illustrated in Fig. 6e, the NbN/TiN@N–C cell maintains an impressive cycling performance of 827.6 mAh/g at 1 C after 500 cycles. Moreover, the long–term cycling stability of the NbN/TiN@N–C–based cell at a high current density of 2 C is shown in Fig. S19 (Supporting information). The battery retains a reversible capacity of 545.5 mAh/g after 1000 cycles, with an exceptionally low capacity decay rate of 0.057 % per cycle. To further assess the practical application potential, the cycling performance of the NbN/TiN@N–C separator was evaluated under high sulfur loading conditions. As shown in Fig. 6f, with a sulfur loading of 8.37 mg/cm^2 and an *E*/*S* value of 7.93 μL/mg, the battery maintains an areal capacity of 3.79 mAh/cm^2 at 0.2 C after 50 cycles.

In summary, a novel heterogeneous catalyst with highly matched NbN/TiN nano–heterocrystals uniformly dispersed within a hollow–porous N–doped carbon framework was successfully synthesized using a facile template and calcination approach. This catalyst was employed as a separator modifier to enhance the performance of Li–S batteries. The heterointerface of the NbN/TiN significantly enhances electron density, leading to stronger interactions with LiPSs and promoting faster electron transfer, as confirmed by DFT calculations. Kinetic tests further demonstrated that the NbN/TiN@N–C composite exhibits a robust chemical affinity for LiPSs, excellent capabilities for rapid Li_2S nucleation and decomposition, and fast charge transfer kinetics. These remarkable properties effectively suppress the shuttle effect caused by soluble LiPSs. Additionally, NbN/TiN@N–C facilitates efficient reversible reactions during the charge/discharge cycles, as evidenced by performance testing and *in–situ* XRD analysis. As a result, cells utilizing the NbN/TiN@N–C modified separator deliver superior rate performance, achieving 663.7 mAh/g at 10 C and exceptional cycling stability with 827.6 mAh/g at 1 C after 500 cycles. This work highlights the catalytic potential of the highly matched heterogeneous strategy and demonstrates the bright promise of heterojunction catalysts for the practical application of lithium–sulfur batteries.

CRediT authorship contribution statement

Xiaoran Li: Writing – original draft. **Wenqian Liu:** Writing – review & editing. **Liwei Zhu:** Writing – review & editing. **Yichun Gu:** Writing – review & editing. **Changhui Sun:** Writing – review & editing. **Peng Wang:** Writing – original draft. **Baojuan Xi:** Writing – review & editing. **Shenglin Xiong:** Writing – review & editing, Conceptualization. **Nianxiang Shi:** Writing – review & editing, Funding acquisition, Formal analysis.

Declaration of competing interest

The authors declare that they have no known competing financial interests or personal relationships that could have appeared to influence the work reported in this paper.

Acknowledgments

This work was financially supported by the Natural Science Foundation of Shandong Province (Nos. ZR2022QB200,

ZR2024MB114), the National Natural Science Foundation of China (Nos. 92572201, U25A20238), the Shandong Provincial University Youth Innovation Science and Technology Support Program (No. 2024KJH126). Thanks to eceshi (www.eceshi.com) for the HRTEM and SAED test. The authors would like to thank Yuru Zhang from SCI–GO (www.sci–go.com) for XPS and XRD date.

Supplementary materials

Supplementary material associated with this article can be found, in the online version, at doi:10.1016/j.cclet.2026.112788.

References

[1] D. Wang, B. Gwalani, D. Wierzbicki, et al., Nat. Mater. 24 (2025) 243–251.
[2] H. Zhang, F. wan, X. Li, et al., Adv. Mater. 37 (2025) 2500950.
[3] H. Wang, X. Lai, C. Chen, et al., Chin. Chem. Lett. 35 (2024) 108473.
[4] B. Li, P. Wang, J. Yuan, et al., Angew. Chem. Int. Ed. 63 (2024) e202408906.
[5] M. Li, H. Liu, Z. Cheng, et al., Adv. Energy Mater. 15 (2025) 2405766.
[6] M. Li, H. Liu, H. Li, et al., Angew. Chem. 64 (2025) e202503174.
[7] Z. Luo, M. Zheng, M. Zhou, et al., Adv. Mater. 37 (2025) 2417321.
[8] G.H. Al–Shawesh, J. Zhu, W. Zhang, et al., Chin. Chem. Lett. 34 (2023) 108190.
[9] H. Ye, J. Lee, Small. Methods 4 (2020) 1900864.
[10] Z. Cui, P. Feng, G. Zhong, et al., Nano–Micro Lett. 18 (2026) 134.
[11] T. Deng, J. Wang, H. Zhao, et al., Adv. Energy Mater. 14 (2024) 2500355.
[12] J. Ke, Z. Wang, H. Zhu, et al., Commun. Mater. 6 (2025) 237.
[13] T. Hou, N. Duan, C. Bi, et al., ACS Nano 19 (2025) 38654–38668.
[14] Z. Yu, M. Liu, D. Guo, et al., Angew. Chem. Int. Ed. 59 (2020) 6406–6411.
[15] J. Yuan, W. Ding, L. Jaishi, et al., Nano Res. 18 (2025) 94907828.
[16] K. Kong, Z. Cheng, X. Ming, et al., Small 21 (2025) 2412586.
[17] Z. Saddam, K. Muthukumar, S. Rajendran, et al., Chem. Eng. J. 519 (2025) 164963.
[18] G. Tang, G. Deng, Z. Jiang, et al., J. Mater. Chem. A 13 (2025) 39775–39784.
[19] Y. Xiang, L. Lu, F. Yan, et al., Carbon Energy 6 (2024) e450.
[20] S. Lu, L. Cai, J. Wang, et al., Small 20 (2024) 2307784.
[21] N. Shi, B. Xi, J. Liu, et al., Adv. Funct. Mater. 32 (2022) 2111586.
[22] C. Ding, Y. Ding, K. Wang, et al., ACS Nano 19 (2025) 26818–26830.
[23] Y. Yu, X. Wang, W. Zhou, et al., Adv. Powder Mater. 4 (2025) 100280.
[24] H. Lu, Y. Su, X. Zhang, et al., Adv. Funct. Mater. 35 (2025) 2425863.
[25] D. Zhang, T. Duan, Y. Luo, et al., Adv. Funct. Mater. 33 (2023) 2306578.
[26] J. Zhu, Y. Xian, F. Liang, et al., Adv. Funct. Mater. 35 (2025) 2425945.
[27] H. Shi, T.Y. Dai, X.Y. Sun, et al., Adv. Mater. 36 (2024) 2406711.
[28] H. Song, T. Nguyen, R. Chu, et al., Nano Energy 128 (2024) 109859.
[29] N. Song, Y. Liang, S. Xiong, et al., Adv. Mater. 37 (2025) e08903.
[30] J. Zhao, H. Cheng, Z. Zhang, et al., Adv. Funct. Mater. 32 (2022) 2202063.
[31] K. Chen, Y. Zhang, Z. Fan, et al., Adv. Funct. Mater. 35 (2025) 2500574.
[32] J. Xu, F. Xie, L. Huang, et al., Nat. Commun. 16 (2025) 4977.
[33] T. Li, G. Nam, K. Liu, et al., Energy Environ. Sci. 15 (2022) 254–264.
[34] J. Lan, G. Hu, Y. Yu, et al., J. Energy Chem. 107 (2025) 792–801.
[35] S. Yang, D. Jiang, Q. Su, et al., Adv. Energy Mater. 14 (2024) 2400648.
[36] F. Ma, Z. Chen, K. Srinivas, et al., J. Energy Chem. 88 (2024) 260–271.
[37] Z. Zhao, Y. Pan, S. Yi, et al., Adv. Mater. 36 (2024) 2310052.
[38] P. Wang, H. Mou, Y. Wang, et al., Angew. Chem. 137 (2025) e202502255.
[39] Q. Jiang, H. Xu, K. Hui, et al., Angew. Chem. Int. Ed. 63 (2024) e202408474.
[40] Y. Lin, J. Wang, X. Zhang, et al., Adv. Funct. Mater. 35 (2025) 2501496.
[41] C. Wang, P. Zhang, J. Li, et al., Nano–Micro Lett. 18 (2026) 7.
[42] J. Guo, L. Chen, L. Wang, et al., Nano–Micro Lett. 18 (2026) 31.
[43] S. Jing, X. Peng, S. Li, et al., Chin. Chem. Lett. 36 (2025) 110732.
[44] T. Wang, J. Zhong, X. Huang, et al., Energy Storage Mater. 81 (2025) 104477.
[45] J. Huang, T. Zhuang, Q. Zhang, et al., ACS Nano 9 (2015) 3002–3011.
[46] Y. Kong, L. Wang, M. Mamoor, et al., Adv. Mater. 36 (2024) 2310143.
[47] Y. Li, H. Liang, J. Guo, et al., Adv. Energy Mater. (2025) 2500355.
[48] Y. Zhao, Z. Shang, M. Feng, et al., Adv. Mater. 37 (2025) 2501869.
[49] Y. Zhuang, H. Yang, Y. Li, et al., ACS Nano 19 (2025) 11058–11074.
[50] X. Kong, Y. Li, G. Cai, et al., Angew. Chem. Int. Ed. 64 (2025) e202510212.
[51] Z. Huang, X. Jiao, J. Lei, et al., Nano Energy 139 (2025) 110979.